Thermoelectric properties of A-site deficient La-doped SrTiO$_3$ at 100-900 °C under reducing conditions

Sathya Prakash Singh[1], Nikola Kanas[1], Temesgen D. Desissa [2*], Mats Johnsson[3], Mari-Ann Einarsrud[1], Truls Norby [2], and Kjell Wiik[1]

[1]Department of Materials Science and Engineering, NTNU Norwegian University of Science and Technology, NO-7491 Trondheim, Norway

[2]Department of Chemistry, Centre for Materials Science and Nanotechnology, University of Oslo, FERMiO, Gaustadalléen 21, NO-0349 Oslo, Norway

[3]Department of Materials and Environmental Chemistry, Arrhenius Laboratory, Stockholm University, S-106 91 Stockholm, Sweden

Keywords: Thermoelectric properties, A-site deficient SrTiO$_3$, grain size, figure-of-merit

Abstract

Lanthanum doped strontium titanate is a potential n-type thermoelectric material at moderate and high temperatures. (La$_{0.12}$Sr$_{0.88}$)$_{0.95}$TiO$_3$ ceramics were prepared by two different routes, conventional sintering at 1500 °C and spark plasma sintering at temperatures between 925 and 1200 °C. Samples with grain size between 40 nm and 1.4 µm were prepared and characterized with respect to their thermoelectric transport properties at temperatures between 100 and 900 ºC under reducing conditions (H$_2$/H$_2$O-buffer mixtures). The thermal conductivity was significantly reduced with decreasing grain size reaching a value of 1.3 W·m^{-1}·K^{-1} at 600 °C for grain size of 40 nm and porosity of 19 %. Electrical conductivity increased with increasing grain size showing a maximum of 500 S·cm^{-1} at 200 °C for a grain size of 1.4 µm. The highest figure-of-merit (*zT*) was measured for samples with 1.4 µm average grain size reaching 0.2 at 500 °C.

1. Introduction

The efficiency of energy systems can be improved by converting waste heat to electricity by thermoelectric generators (TEGs). These are silent and compact but have limited efficiencies as well as stability challenges under high temperature operation [1, 2]. The efficiency of a given

---

* Present address: Department of Materials Science and Engineering, Adama Science and Technology University, P.O.Box: 1888, Adama, Ethiopia.

thermoelectric (TE) material can be calculated by the dimensionless figure of merit, zT [3] as shown in Eq. 1

$$zT = \frac{S^2 \sigma T}{\kappa} \qquad (1)$$

where S is the Seebeck coefficient (thermoelectric power), σ is the electrical conductivity, T is the absolute temperature, and κ is the total thermal conductivity corresponding to the sum of electronic and lattice contributions. For applications of thermoelectric generators where maximum electrical power generation is of importance (infinite heat source) the material selection should be focused on materials with high power factor, $P = S^2 \sigma$, and the reduction in thermal conductivity becomes less important [4-6]. For applications where maximum conversion efficiency is the key factor (limited heat source) the optimization of zT is still important [5]. In the literature survey below the different material systems are distinguished with respect to the highest achieved figure-of-merit.

The state-of-the-art thermoelectric materials are represented by tellurides such as Bi_2Te_3 and Sb_2Te_3 [7-8] with zT values well above 2. These systems are representative for a number of thermoelectric materials based on heavy, toxic and rare metals and combined with low melting temperature and oxidation in air, these materials are ruled out for applications in oxidizing atmosphere at elevated temperatures. In contrast, a number of oxide based thermoelectric materials are nontoxic, stable in oxidizing atmosphere even at high temperatures and made of abundant and less expensive elements, which make them candidate materials for high temperature applications. However, the TE-properties of oxides are still inferior to the metallic based systems and the thermoelectric properties need to be improved.

Whereas oxides with *p-type* electrical conductivity, such as Na_xCoO_2 and $Ca_3Co_{4-x}O_{9+\delta}$, show zT-values above the threshold value 1 [9] and ≈ 0.7 [10], respectively, the *n-type* TE-oxides still suffer from low to moderate zT-values. The most promising backbone structures for *n-type* oxides are ZnO [11], $CaMnO_3$ and $SrTiO_3$ (STO) [12], however oxygen deficient fluorite derivative $Ga_{3-x}In_{5+x}Sn_2O$ oxides also show promising performance with zT=0.28 at 727 °C [13]. Koumoto *et al.* [14] and Walia *et al.* [15] have given general reviews on thermoelectric properties of a variety of oxides while an updated review on STO based ceramics is given below.

Undoped STO shows poor to moderate thermoelectric performance even in reducing atmosphere [16-21] and donor doping on the A- and B-site is a common approach to enhance the TE-properties. The variation in zT for La-doped STO has been reported in [22-24] showing zT values between 0.16 and

0.37. The highest zT was reported by Kikuchi *et al.* [23] reaching 0.37 at 772 ℃ based on spark plasma sintered (SPS) combustion synthesized powder. Ekren *et al.* [4] doped STO with 10 % Nd on A-site and added small amounts of ZrO_2 and B_2O_3 to increase electrical conductivity and promote densification by liquid phase sintering, respectively They reported a significantly enhanced power factor and zT reached 0.37 at 742 ℃.

Nb as a B-site dopant has been investigated in [25-27] and Zhang *et al.* [26] reported zT=0.40 at 827 ℃ for sintered samples where small amounts of a secondary phase were observed (possibly TiO_2). Li *et al.* [28] have reported the highest zT values to date for a bulk STO material co-doped with La and Nb. They reported values between 0.41 and 0.43 at temperatures between 496 and 736 ℃. Their powder precursors were produced by a hydrothermal method and minor amounts of carbon powder was added prior to sintering by hot pressing. Sintered samples contained small amounts of secondary phases corresponding to TiO_2 and NbC.

The possibility of A-site deficiency in doped/co-doped STO has attracted attention from several research groups [29-36]. Azough *et al.* [29] investigated the variation in thermoelectric properties of $Sr_{1-x}La_{2x/3}TiO_{3-\delta}$ with x between 0.0 and 0.9. They infer that A-site vacancies are randomly distributed at $x<0.3$, vacancy clustering occurred at intermediate x and finally ordering of both A-site vacancies and La at x=0.9. They show that increasing x significantly reduce the thermal conductivity, while the highest electronic conductivity was reported for x= 0.3 and the lowest for x=0.9. zT reached 0.27 at 800 ℃ for x=0.5. Lu *et al.* [33] made a similar study as Azough *et al.* [29] although using a different notation for the La-doped A-site deficient STO: $Sr_{1-3y/2}La_yTiO_{3-\delta}$. They reported the thermoelectric properties of sintered samples varying y between 0 and 0.30 and reached zT=0.41 at 700 ℃ for y= 0.15 (equal to x= 0.225 using Azough´s notation). The most obvious reason for the discrepancy between these two reports is most likely the electrical conductivity which is much higher in Lu et al.´s samples and may originate from differences in pO_2.

A-site deficient STO co-doped with La and Nb is reported in [30, 32, 35], and the highest zT was achieved by Srivastava *et al.* [30] reaching 0.35 at 727 ℃. Chen *et al.* [34] co-doped A-site deficient STO with Nd and Nb and obtained zT=0.32 at 800 ℃. They observed a significant reduction in thermal conductivity with increasing concentration of Sr-vacancies.

In the present investigation we take advantage of the encouraging results related to A-site deficient, donor doped STO [29, 33]. Our prime aim is to investigate the variation in TE properties (σ, S, κ and zT) with grain size, porosity and temperature in reducing atmosphere. STO-materials with

4

5 mol% A-site deficiency, corresponding to the nominal stoichiometry $(La_{0.12}Sr_{0.88})_{0.95}TiO_{3-\delta}$ (LSTO), alternatively written as $La_{0.11}Sr_{0.84}VA_{0.05}TiO_{3-\delta}$, where VA is cation vacancies on A-site was selected. The TE properties are reported for materials with grain size varying between 40 nm and 1.4 μm at temperatures between 100 and 900 ^{o}C.

2. Materials and Methods

Dense ceramic samples with grain size ranging from 40 nm to 0.8 μm were prepared from powders produced by spray pyrolysis (SP) and densified by spark plasma sintering (SPS) (Dr. Sinter 2050 SPS, Sumitomo Coal Mining Co., Tokyo, Japan). Synthesis and sintering procedure are described more in detail by Loland *et al.* [37]. Samples with average grain size 1.4 μm were based on powders prepared by solid state reaction (SSR). Stoichiometric amounts of dried La_2O_3 (99.9 %), TiO_2 (99.9 %) and $SrCO_3$ (99.9 %) (Inframat Advanced Materials), were mixed using a planetary mill for 60 min with yttria-stabilized zirconia (YSZ) balls in isopropanol followed by drying in a Rotavapor and heat treatment at $\sim$120 °C to produce a dry powder. The resulting powder was calcined at 1100 °C for 7 h in an alumina crucible and subsequently ground and sieved. Disc- and bar-shaped samples were prepared using uniaxial pressing followed by cold isostatic pressing (CIP) at 200 MPa and finally sintered at 1500 °C in 5 % H_2/95 % N_2 for 4 h. Heating and cooling rates were 200 °C/h. Density and porosity were determined by the Archimedes method using isopropanol and $\rho_{theor,LSTO}$=5.160 g/cm^3 [37]. Phase purity was analyzed on sintered and ground samples by powder X-ray diffraction (XRD) (Bruker D8 DaVinci 1 diffractometer). SPS samples sintered at 925 and 1100 ^{o}C resulted in small grains, and crystallite size was determined by XRD based on the solution of the Scherrer equation [37], which can be used for crystallites less than 200 nm. The SPS sample sintered at 1200 ^{o}C was prepared by tripod wedge polishing before subjected to TEM analysis and scanning TEM (STEM) images were recorded to reveal both grain size (linear intercept method) and the presence of secondary phases by EDS analysis. The sample sintered (SSR) at 1500 ^{o}C was carefully polished and subjected to thermal etching (10 min at 1400 ^{o}C) to reveal the grain boundaries and the grain size was estimated based on scanning electron microscopy (SEM, Hitachi S-3400N) using the linear intercept method. Electrical conductivity was measured by the 4-point DC-method (homemade setup [38]) and Seebeck coefficient measurements were done using a ProboStat (NORECS, Norway). All electrical characterization (conductivity and Seebeck) was done on bar shaped samples (20·3·3 mm^3) in humidified atmosphere (3 % H_2O in 5 % H_2/Ar) at 1 atm total pressure, corresponding to

variation in oxygen partial pressures between $8 \cdot 10^{-29}$ and $2 \cdot 10^{-17}$ atm at temperatures between 500 and 900 °C. The humidified atmosphere was chosen to establish a defined partial pressure of oxygen (pO_2) at each temperature, as opposed to a dry non-buffered atmosphere with an undefined pO_2. The samples were equilibrated at high temperature (800 or 900 °C) before the temperature was decreased stepwise by 100 °C intervals for each measured value recorded. Residence time at each temperature was sufficiently long to establish thermal equilibrium. The thermal conductivity (κ) was calculated from the product of thermal diffusivity (D), specific heat capacity (C_p) and density (ρ), $\kappa = DC_p\rho$, where the thermal diffusivity was measured by the laser flash method (Netzsch LFA 457 MicroFlash) on disc shaped samples (diameter=12.2 mm, thickness=2.5 mm).

3. Results and Discussion

3.1. Phases and microstructure

Powder XRD patterns of the sintered materials given in Fig. 1 show the main cubic $SrTiO_3$ phase along with small amounts of secondary phases. $La_2Ti_3O_9$ is observed in all samples, in addition to observation of a TiO_2-phase at both 1200 °C (rutile) and 1500 °C (anatase). Since both TiO_2 and $La_2Ti_3O_9$ are observed in materials sintered at 1200 and 1500 °C, it is anticipated that these phases to coexist with the main cubic $SrTiO_3$-based phase. The presence of TiO_2 at lower temperatures cannot be ruled out, however, if present, the amount is below the XRD detection limit. Since anatase is the low temperature modification of TiO_2, while rutile is the stable phase at higher temperatures [39], the opposite observation in this case remains unexplained.

Density and grain size of the sintered materials are given in Tab. 1. There is a significant increase in grain size with temperature and the porosity is low for samples sintered at 1100°C and above, while a rather high porosity (19 %) is observed for the sample sintered at 925 °C. Microstructures of samples sintered at 1200 and 1500 °C are presented in Fig. 2.
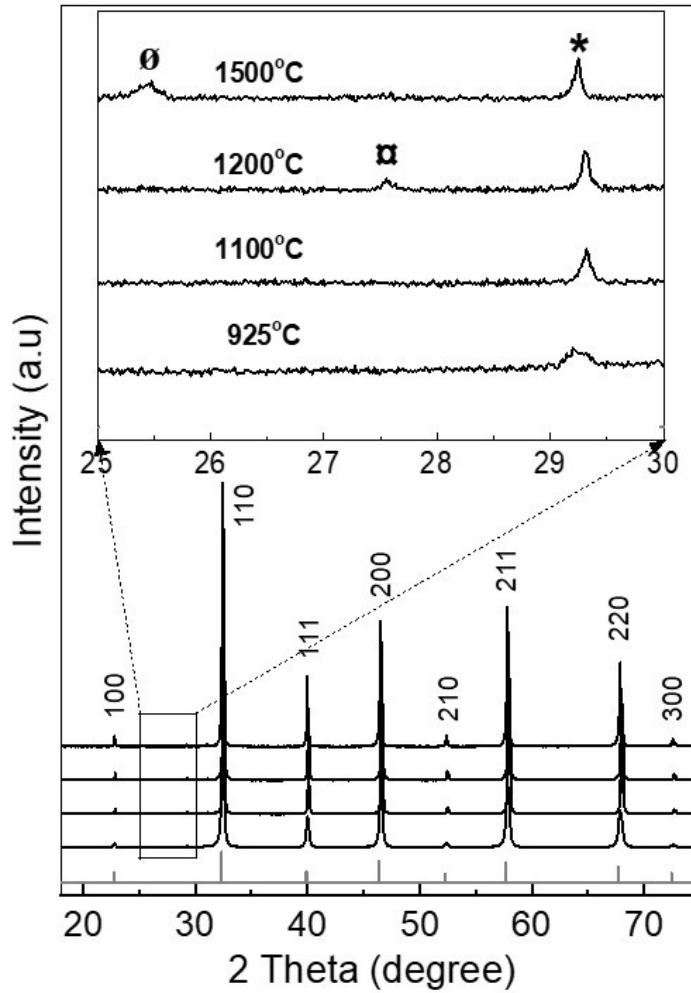
Figure 1. XRD pattern of $(Sr_{0.88}La_{0.12})_{0.95}TiO_3$ sintered at 925, 1100, 1200 and 1500 °C. Secondary phases are marked: $La_2Ti_3O_9$ (*): 29.3 °, PDF:01-075-4857) and TiO_2 (ø), 25.4 ° PDF:01-086-1155 (Anatase-tetragonal), TiO_2 (¤) 27.5 °, PDF:04-003-0648, (Rutile). Main phase $La_{0.10}Sr_{0.90}TiO_3$ (with Miller indices and indicated with grey vertical lines at the abscissa PDF: 04-002-1010), and the peak at 2 theta equal 31.1 ° is due to the instrument (secondary radiation from tungsten ($WLa_{\alpha1}$) originating from the X-ray tube).
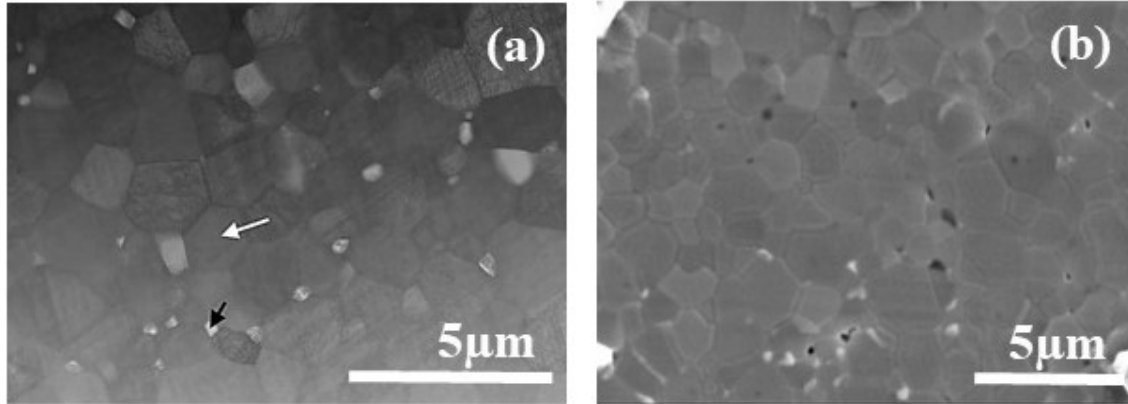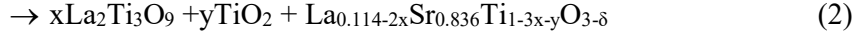
Figure 2. a) STEM image of sample sintered at 1200 °C. The black arrow points at a secondary TiO$_2$-rich grain (EDS analysis) while the white arrow points at the main LSTO phase. b) SEM image of sample sintered at 1500 °C (polished and thermally etched).

Table 1. Sintering method, sintering temperature, grain size and density for the (La$_{0.12}$Sr$_{0.88}$)$_{0.95}$TiO$_3$ materials.

Sintering		Grain size	Density (%)	Powder preparation method
Method	Temperature (°C)			
SPS	925	40 nm	81	Spray pyrolysis
	1100	130 nm	97	
	1200	0.8±0.1 μm	99	
SSR	1500	1.4±0.1 μm	99	Solid state reaction

Heating the material with nominal stoichiometry (La$_{0.12}$Sr$_{0.88}$)$_{0.95}$TiO$_{3-\delta}$ yielded small amounts of secondary phases. The solid solubility of La$_2$O$_3$ in STO is significant [40] and the presence of secondary phases may be due to A-site deficiency. Several research groups [26, 28, 30, 33, 41-42] have observed the presence of secondary phases in donor doped STO both for A-site deficient and stoichiometric compositions and a systematic study of phase relations and stability in the LSTO system has not yet been encountered in the literature. Considering the presence of secondary phases, the final stoichiometry of our materials may be described by Eq. 2,

$$0.057La_2O_3 + 0.836SrO + TiO_2 \rightarrow (La_{0.12}Sr_{0.88})_{0.95}TiO_{3-\delta}$$

$$\rightarrow x\mathrm{La_2Ti_3O_9} + y\mathrm{TiO_2} + \mathrm{La_{0.114-2x}Sr_{0.836}Ti_{1-3x-y}O_{3-\delta}} \tag{2}$$

suggesting that the final composition represents the equilibrium composition which will be established at least at high temperatures. *x* and *y* in Eq. 2 are unknown and the possible consequence with respect to the final stoichiometry of the LSTO phase will not be treated further. The materials will simply be referred to using the nominal stoichiometry $(\mathrm{La_{0.12}Sr_{0.88}})_{0.95}\mathrm{TiO_{3-\delta}}$ or alternatively $\mathrm{La_{0.11}Sr_{0.84}VA_{0.05}TiO_{3-\delta}}$.

3.2. Electrical conductivity

Electrical conductivities of the STO-based materials are presented in Fig. 3a. The relaxation time at temperatures above 400 °C was at least 8 h. At temperatures below 400 °C, the relaxation time was rather short due to low mobility of defects such as oxygen- and Sr-vacancies, corresponding to a "frozen-in" state. Since the porosity also affects the measured electrical conductivity, the conductivity of the material with the highest porosity (19 %) was adjusted using the Landauer equation [43].

$$\sigma = \sigma_m \frac{1}{(1-p)^{\frac{3}{2}}} \tag{3}$$

where σ_m is the measured electrical conductivity, p is the fraction of pores and σ is the calculated electrical conductivity for a non-porous material. Taking the porosity into account, a moderate upward shift in electrical conductivity is observed (gray square symbols in Fig. 3a). Whereas the 40 nm sample shows a pronounced increase in electrical conductivity with temperature in the whole temperature interval, the electrical conductivity of samples with grain sizes 130 nm and 0.8 µm are virtually independent of temperature above 300 °C. Further increase in grain size to 1.4 µm gave the highest conductivity at all temperatures, however with a pronounced decrease at temperatures above 300 °C. At temperatures below approx. 700 °C, the conductivity is significantly enhanced with increasing grain size, which is also evident in Fig. 3b where the isothermal electrical conductivity is plotted against grain size.
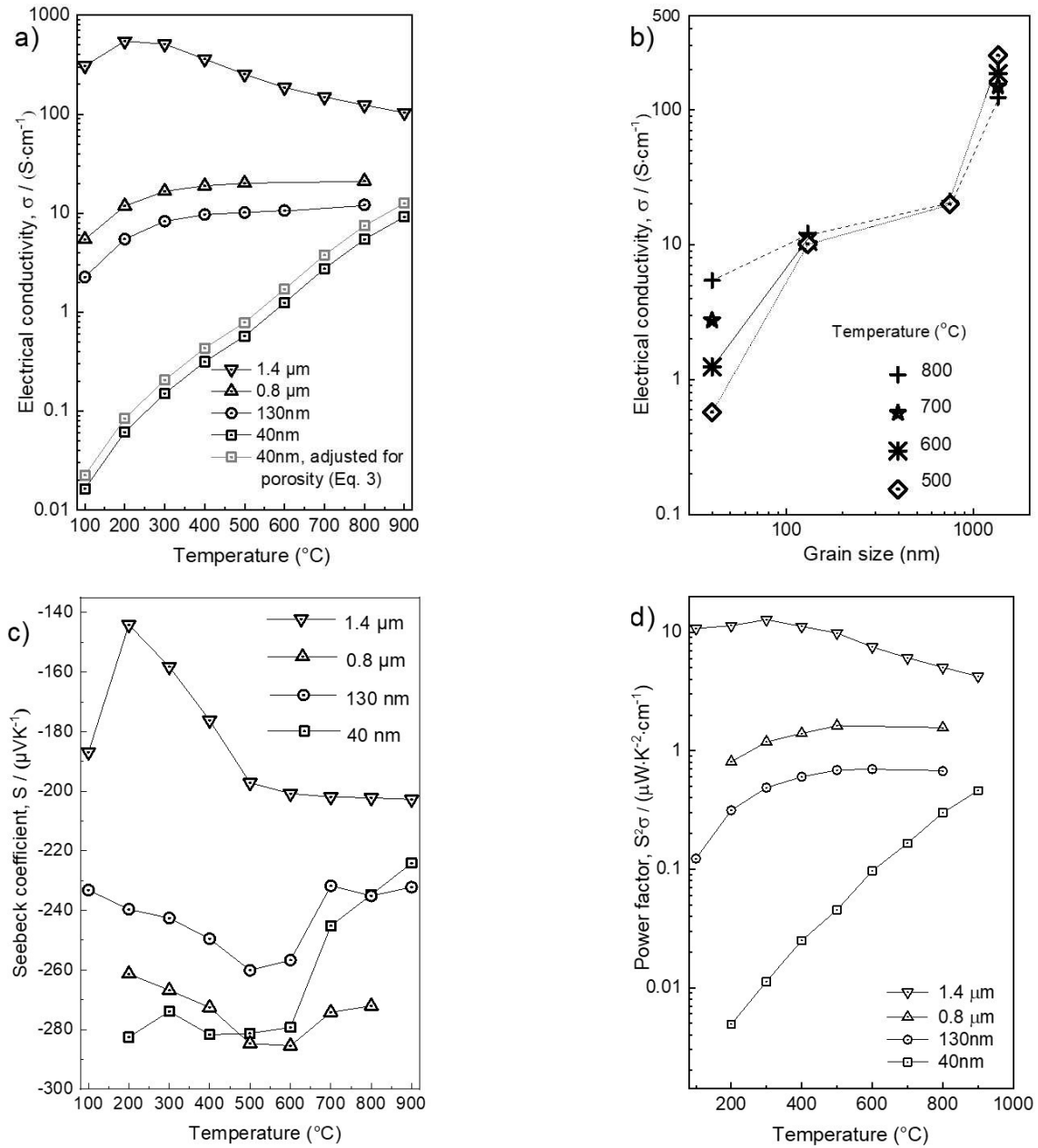
Figure 3. a) Temperature dependence of electrical conductivity. The uncertainty in conductivity is ±1 %. b) Isothermal electrical conductivity as a function of grain size. c) Temperature dependence of the Seebeck coefficient, S. Uncertainty within ±5 %. d) Power factor, P, as a function of temperature.

The defect chemistry of La-doped STO is one important key to understand the variation in electrical conductivity with temperature and partial pressure of oxygen (pO_2) and is extensively treated by

e.g. Moos *et al.* [40, 44-45] and Blennow *et al.* [46]. A simple approach to n-type electronic conductivity in oxides is given by the formation of oxygen vacancies ($V_o^{\bullet\bullet}$) and charge compensating defect electrons (e'),

$$O_o^x = V_o^{\bullet\bullet} + 2e' + \frac{1}{2}O_2 \qquad (4)$$

where O_o^x is an oxide ion on its regular site. According to Eq. 4 the electronic conductivity should increase with decreasing pO_2 at constant temperature and increase with temperature at constant pO_2. However, it is well established that A-site deficiency, *i.e.*, Sr-vacancies ($V_{Sr}^{//}$), plays a crucial role with respect to the electrical properties both in pure- and donor-doped STO [44], and the same goes for three-valent cations such as lanthanum as a donor dopant on A-site ($La_{Sr}^{\bullet}$), so that the total electroneutrality condition, Eq. 5 may be written

$$n = \left[La_{Sr}^{\bullet} \right] + 2\left[V_o^{\bullet\bullet} \right] - 2\left[V_{Sr}^{//} \right] \qquad (5)$$

where *n* is the concentration of electrons. Moos *et al.* [45] showed that at some intermediate pO_2 the concentration of electronic charge carriers was defined by the dopant level of La in STO, corresponding to Eq. 6.

$$n = \left[La_{Sr}^{\bullet} \right] \qquad (6)$$

With a fixed value of *n*, the temperature variation of σ will be dictated by the variation in mobility of the electronic species, μ_n, and according to [45] the mobility follows a variation with temperature described by Eq. 7,

$$\mu_n(T) = \mu_0 \cdot \left(\frac{T}{K} \right)^{-M} \qquad (7)$$

where μ_o is (field) mobility at nominal temperature, and *M* is an exponent, independent of temperature, but increases monotonously with the lanthanum content. The material with the largest grain size (1.4 μm) shows a decreasing conductivity with increasing temperature above 300 ℃ (Fig. 3a) and is well explained by the derivation given above. The same characteristic variation in σ with temperature under reducing atmosphere has been observed by several research groups for A-site deficient, donor doped STO [28-30, 33-35, 41-42].

However, for the materials sintered by SPS (40 nm, 130 nm and 0.8 μm) the conductivity *vs.* temperature deviates significantly from the characteristic behaviour explained above. The 40 nm material showed an increase in electrical conductivity with increasing temperature, while the overall electrical conductivity was lower than for the other materials at all temperatures. The materials with grain size 130 nm and 0.8 μm show a similar behaviour, increasing conductivity with temperature at $T<500$ °C, however becoming apparently independent at even higher temperatures. Ohta *et al.* [25] investigated the effect of grain size (200 nm, 20 μm, and single crystal) on the thermoelectric performance of Nb-doped STO. The concentration of charge carriers was found to be constant and independent of temperature. However, for materials with grain size 200 nm they observed a low electrical conductivity at low temperatures followed by a steep increase with increasing temperature. They explained their observations by the formation of a double Schottky barrier (DSB) at the interface between the grains which would reduce the carrier mobility significantly at low temperatures. The width of the DSB was shown to decrease with increasing temperature leading to an increase in mobility corresponding to enhanced electrical conductivity. Single crystal and materials with grain size 20 μm showed a gradual decrease in mobility over the whole temperature range (10-1000 K). Although Ohta *et al.* [25] investigated Nb-doped STO we suggest that a similar mechanism explains the conductivity behaviour also in the samples sintered by SPS, corresponding to a reduced conductivity with increased density of grain boundaries. Ekren *et al.* [4] have also acknowledged grain boundaries as scattering centres for charge carriers and that a more uniform microstructure will improve carrier mobility. Comparable behaviour has been observed by Roy *et al.* [47], for Nb-doped STO sintered by SPS for 5 min at temperatures between 1250 and 1500 °C.

Segregation at grain boundaries may also affect the electrical conductivity. Longworth *et al.* [48] observed a depletion of La at the grain boundaries for La-doped STO, which again will increase the electrical resistivity at the grain boundaries. Dehkordi *et al.* [49], on the other hand, investigated the variation in thermoelectric properties of Pr-doped STO and observed enhanced carrier mobility originating from the formation of Pr-rich grain boundaries. Hence, [48-49] emphasize the importance of segregation of the dopants on the electrical conductivity.

According to the XRD analysis (Fig. 1) it is evident that secondary phases ($La_2Ti_3O_9$ and TiO_2) are formed during sintering. For samples sintered at 1200 °C, TEM/EDS analysis also show the formation of TiO_2 at triple points between the LSTO grains (Fig. 2 c). It is anticipated that the electronic conductivity of the secondary phases is lower than the main LSTO phase, and the effect on the measured electrical conductivity will depend on whether the secondary phases are formed

mainly at triple points or at the grain boundaries. Formation at the grain boundaries will be the most detrimental to the electrical conductivity due to the separation of the grains with a phase with a lower conductivity. A more elaborate TEM study is however needed to locate the distribution of secondary phases in detail.

3.3. Seebeck coefficient

The Seebeck coefficients, S, presented in Fig. 3c are all negative, confirming *n-type* conductivity for all the materials at the given conditions. The variation in S was in the range from almost -140 $\mu V \cdot K^{-1}$ to approx. -270 $\mu V \cdot K^{-1}$. For metals or degenerate semiconductors, the relationship between S and carrier concentration, n, is given by Eq. 8 [50],

$$S = \frac{8\pi^2 k_B^2}{3eh^2} m^* T (\frac{\pi}{3n})^{\frac{2}{3}} \qquad (8)$$

where k_B is the Boltzmann constant, e is the elementary charge, h is Plank's constant, m^* is the effective mass of charge carrier, and T is the absolute temperature. Hence, $|S|$ is inversely proportional to the carrier concentration ($n^{-\frac{2}{3}}$), which is reasonably fulfilled for the material with grain size 1.4 μm according to Fig. 3a and 3c. The Seebeck coefficients are also in the same range as reported for $La_{0.12}Sr_{0.88}TiO_3$ by Shang *et al.* [24], as their values were in the range -80 to -180 $\mu V \cdot K^{-1}$ measured between room temperature and 700 °C. The materials with grain size 40 nm show a significantly higher $|S|$ due to the low σ (Fig. 3a) and a decreasing $|S|$ with increasing temperature in correspondence with the conductivity given in Fig. 3a. The materials with grain size 130 nm and 0.8 μm show a more anomalous behaviour, apparently with a maximum in $|S|$ around 500 °C. The variation in $|S|$ for these materials contradicts the proportionality predicted by Eq. 8. However, considering the ±5 % uncertainty, the variation in $|S|$ between the materials with grain size ranging from 40 nm to 0.8 μm is relatively small.

3.4. Power factor ($P = \sigma S^2$)

The power factor in terms of temperature for all samples is shown in Fig. 3d. Although the variation in the measured Seebeck coefficients was significant (Fig. 3c), the relative variation in power factor is dictated by the electrical conductivity as evidenced by comparing Figs. 3a and 3d. The material with the 1.4 μm grain size stands out with a considerably higher power factor than any of the other materials, reaching almost 13 $\mu W \cdot K^{-2} \cdot cm^{-1}$ at 300 °C, comparable with 15 $\mu W \cdot K^{-2} \cdot cm^{-1}$ achieved by Azough *et al.* [29] at 200 °C for a similar composition. Even

higher power factors have been reported by Ekren *et al.* [4] reaching 20 $\mu W \cdot K^{-2} \cdot cm^{-1}$ at 227 °C for Nd-doped STO, essentially due to the high electrical conductivity (1100 $S \cdot cm^{-1}$) at the same temperature. This emphasize the potential of donor doped STO in applications where electrical power generation is of importance [5-6].

3.5. Thermal conductivity

The thermal conductivity, κ, presented in Fig. 4a shows decreasing values with temperature, in accordance with scattering governed by the mean free path of the phonons (a *1/T* proportionality). Whereas the thermal conductivity of the materials with grain size 0.8 and 1.4 μm is similar and shows a high value, a distinct reduction in κ is observed for the sample with grain size of 130 nm. Reducing the grain size further to 40 nm and introducing porosity gave another significant reduction in thermal conductivity showing the lowest value of 1.3 $W \cdot m^{-1} \cdot K^{-1}$ at 600 °C. Wang *et al.* [19] investigated the variation in κ for nanograined SrTiO$_3$ (prepared by SPS) and showed a theoretical minimum of 1.4 $W \cdot m^{-1} \cdot K^{-1}$ for 10 nm grains just above room temperature. Loland *et al.* [37] modelled the expected variation in κ with grain size and porosity for SrTiO$_3$ at 1000 K based on data published by Wang *et al.* [19]. A 40 % increase in κ was estimated for 100 nm grain size for an increase in density from 81 to 100 %, emphasizing a significant contribution from pores with respect to reducing the thermal conductivity. Assuming that a 40 % increase is a reasonable estimate also for our 40 nm sample the thermal conductivity would increase from 1.3 to 1.8 $W \cdot m^{-1} \cdot K^{-1}$ assuming a shift in density from 81 to 100 %. It should also be emphasized that κ will be reduced by the presence of Sr-vacancies in combination with La-dopant (heavy element) [29, 34], suggesting that 40 % is somewhat overestimated.

According to the XRD-analysis (Fig. 1), the presence of secondary phases is more dominating for the 0.8 and 1.4 μm materials and for that matter it seems that grain size and porosity is more decisive for κ than the presence of secondary phases in this case.

3.6. Figure-of-merit (zT)

Fig. 4b presents *zT* values for all the materials in the present study. The 1.4 μm material exhibited the overall highest *zT* with a peak value of 0.2 at 500 °C. Including the presence of A-site vacancies the stoichiometry may be written as $Sr_{0.84}La_{0.11}VA_{0.05}TiO_{3-\delta}$, which corresponds to *x*=0.16 in Azough *et al.*´s [29] notation ($Sr_{1-x}La_{2x/3}TiO_{3-\delta}$) and *y*=0.11 in Lu *et al.*´s [33] notation ($Sr_{1-3y/2}La_yTiO_{3-\delta}$). For the same stoichiometry and temperature (500 °C)

there is close agreement between zT=0.2 and their reported values, with the distinction that Lu *et al.* reach approx. 0.3 at higher temperatures (700 °C). However, Lu *et al.* reported even higher zT values for materials with nominal stoichiometry $Sr_{0.775}La_{0.15}VA_{0.075}TiO_{3-\delta}$, ranging from zT=0.2 at 500 °C to 0.4 at 700 °C. The high zT-values are due to the high electronic conductivity varying from 750 S·cm^{-1} at 500 °C to 400 S·cm^{-1} at 700 °C.

Whereas the material with 1.4 µm grain size showed the highest zT, the 40 nm material exhibited the lowest values. Even though the thermal conductivity was significantly reduced by smaller grain size, this was on the expense of the electrical conductivity, and the resulting zT values became low.
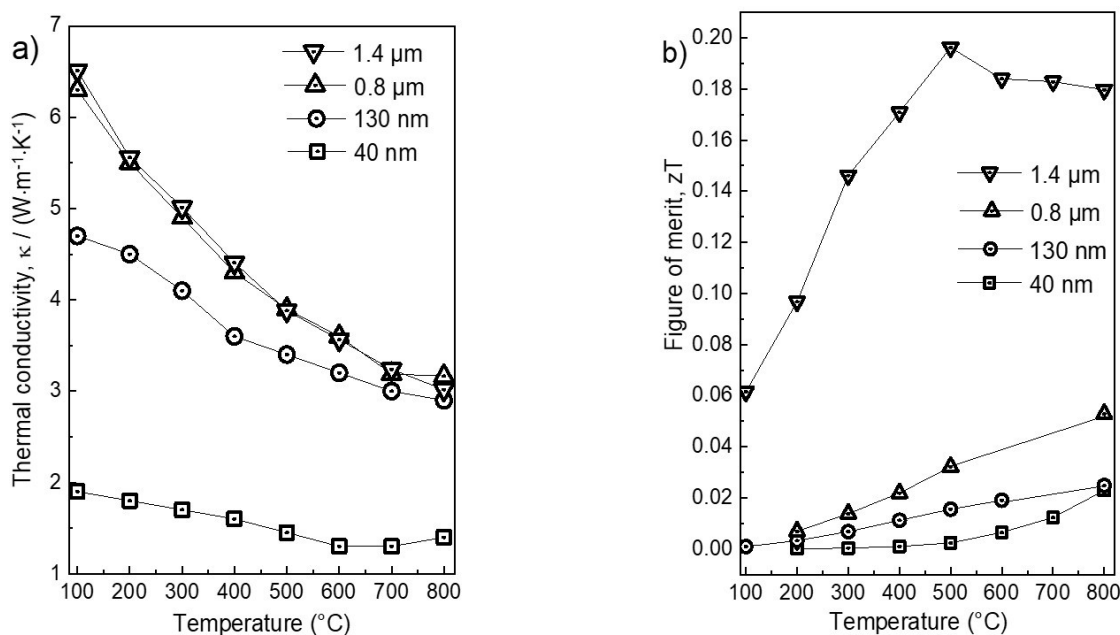

Figure 4. a) Thermal conductivity, κ, as a function of temperature. The uncertainty in the thermal conductivity values is ±6 %. b) Temperature dependence of the dimensionless figure-of-merit, zT.

To take advantage of the reduced thermal conductivity due to nano-sized grains, measures are necessary to significantly reduce the electrical resistance represented by grain boundaries. This may be accomplished by introducing alternative donor dopants which are enriched (segregated) at the grain boundaries [49] rather than depleted [48]. Still, challenges may be encountered associated with the formation of a double Schottky barrier (DSB) at the interface between the grains as pointed out by Ohta *et al.* [25].

Materials with grain size 40 nm to 0.8 μm were sintered by SPS (high pressure and short time), while the materials with grain size 1.4 μm were sintered conventionally. Applying SPS, the driving force for mass transport will be enhanced and it is also commonly assumed that the grain surfaces become cleaner due to the formation of a plasma between the grains during sintering. This mechanism is not active in conventional sintering, and it cannot be ruled out that these differences also may affect the thermoelectric properties of the materials. From Fig. 1 it is observed that the phase distribution in the materials sintered at 1200 °C (SPS) and 1500 °C (conventional) is very similar, except that rutile was formed at 1200 and anatase at 1500 °C. Whether this may affect the TE properties remain speculation and can only be answered by doing a further comparative study with focus on the role of the sintering method with respect to TE properties.

Finally, the many research reports on STO based materials give some promise to future exploration of this material system for applications in thermoelectric devices at high temperatures. Nevertheless, it should be emphasized that from an application point of view, devices assembled with STO based materials are restricted to reducing conditions and high temperatures, which complicates operation in ambient atmospheres.

4. Conclusion

$(La_{0.12}Sr_{0.88})_{0.95}TiO_3$ materials were prepared by two different routes, conventional sintering at 1500 °C and spark plasma sintering at temperatures between 925 and 1200 °C. TE properties, were measured on samples with grain size ranging from 40 nm to 1.4 μm in reducing atmosphere (H_2/H_2O-buffer mixtures) in the temperature range from 100 to 900 °C. The thermal conductivity, κ, was significantly reduced with decreasing grain size, and the lowest thermal conductivity was observed for samples with grain size of 40 nm reaching 1.3 W·m^{-1}·K^{-1} at 600 °C. The reduction in thermal conductivity was due to a combination of nanosized grains and porosity. The electrical conductivity, σ, increased with grain size signifying the resistive nature of the grain boundaries. The highest figure-of-merit, zT =0.2, was measured at 500 °C for the sample with grain size of 1.4 μm and was dictated by a high electrical conductivity compared to samples with smaller grains. To take advantage of the reduced thermal conductivity due to nano-sized grains, it is concluded that measures, such as appropriate doping, are necessary to significantly reduce the electrical resistance represented by grain boundaries.

Acknowledgements

References

1. T. M. Tritt, Thermoelectric phenomena, materials, and applications. *Annu. Rev. Mater. Res.*, 2011. 41: p. 433-48.

2. K. Koumoto, W. Yifeng, R. Zhang, A. Kosuga, and R. Funahashi, Oxide thermoelectric materials: A nanostructuring approach. *Annu. Rev. Mater. Res.,* 2010. 40: p. 363-94.

3. A. Bulusu, and D. G. Walker, Review of electronic transport models for thermoelectric materials. *Superlattices and Microstruct.*, 2008. 44: p. 1-36.

4. D. Ekren, F. Azough, A. Gholinia, S. J. Day, D. Hernandez-Maldonado, D. M. Kepaptsoglou, Q. M. Ramasse, R. Freer, Enhancing the thermoelectric power factor of $Sr_{0.9}Nd_{0.1}TiO_3$ through control of the nanostructure and microstructure, *J. Mater. Chem. A,* 2018. 6: p. 24928-24939.

5. M. Bittner, N. Kanas, R. Hinterding, F. Steinbach, J. Räthel, M. Schrade, K. Wiik, M.-A. Einarsrud and A. Feldhoff, A comprehensive study on improved power materials for high-temperature thermoelectric generators, *Journal of Power Sources*, 2019. 410-411: p. 143-151.

6. M. Bittner, N. Kanas, R. Hinterding, F. Steinbach, D. Groeneveld, P. Wemhoff, K. Wiik, M.-A. Einarsrud and A. Feldhoff, Triple-phase ceramic 2D nanocomposite with enhanced thermoelectric properties, *J. Eur. Ceram. Soc.*, 2019. 39: p. 1237-1244.

7. R. Venkatasubramanian, E. Siivola, T. Colpitts, and B. O'Quinn, Thin-film thermoelectric devices with high room-temperature figures of merit. *Nature*, 2001. 413: p. 597-602.

8. D. A. Polvani, J. F. Meng, N. V. Chandra Shekar, J. Sharp, and J. V. Badding, Large improvement in thermoelectric properties in pressure-tuned p-type $Sb_{1.5}Bi_{0.5}Te_3$. *Chem. Mater.*, 2001. 13(6): p. 2068-2071.

9. K. Fujita, T. Mochida, K. Nakamura, High-temperature thermoelectric properties of $Na_xCoO_{2-\delta}$ Single Crystals. *Jpn. J. Appl. Phys.*, 2001. 40(7R): p. 4644-4647.

10. S. Saini, H. S. Yaddanapudi, K. Tian, Y. Yin, D. Magginetti, A. Tiwari, Terbium ion doping in $ca_3co_4o_9$: A step towards high-performance thermoelectric materials. *Sci. Rep.*, 2017. 7: p. 44621-9.

11. L. Han, D. V. Christensen; A. Bhowmik, S. B. Simonsen, L. T. Hung, E. Abdellahi, Y. Z. Chen, N. V. Nong, S. Linderoth, N. Pryds, Scandium-doped zinc cadmium oxide as a new stable n-type oxide thermoelectric material. *J. Mater. Chem. A*, 2016. 4(31): p. 12221-12231.

12. J. W. Fergus, Oxide materials for high temperature thermoelectric energy conversion. *J. Eur. Ceram. Soc.*, 2012. 32(3): p. 525-540.

13. S. D. Bhame, T. Zhou, E. Guilmeau, Y. Kinemuchi, F. Delorme, B. Raveau, Synthesis and thermoelectric properties of oxygen deficient fluorite derivative $Ga_{3-x}In_{5+x}Sn_2O_{16}$. *J. Appl. Phys.*, 2010. 108(9): p. 093708-4.

14. K. Koumoto, R. Funahashi, E. Guilmeau, Y. Miyazaki, K. A. Weidenkaff, Y. Wang, and C. Wan, Thermoelectric ceramics for energy harvesting. *J. Am. Ceram. Soc.*, 2013. 96(1): p. 1-23.

15. S. Walia, S. Balendhran, H. Nili, S. Zhuiykov, G. Rosengarten, Q. H. Wang, M. Bhaskaran, S. Sriram, M. S. Strano, and K. K. Zadeh, Transition metal oxides – Thermoelectric properties. *Prog. Mater. Sci.*, 2013. 58(8): p. 1443-1489.

16. J. U. Rahman, W. H. Nam, N. V. Du, G. Rahman, A. U. Rahman, W. H. Shin, W.-S. Seo, M. H. Kim, S. Lee, Oxygen vacancy revived phonon-glass electron-crystal in $SrTiO_3$, *Journal of the European Ceramic Society,* 2019. 39: p. 358-365.

17. H. Muta, K. Kurosaki, S. Yamanaka, Thermoelectric properties of reduced and La-doped single-crystalline $SrTiO_3$, *Journal of Alloys and Compounds*, 2005. p. 306-309.

18. L. Feng, T. Shiga, J. Shiomi, Phonon transport in perovskite $SrTiO_3$ from first principles, *Applied Physics Express,* 2015. 8, 071501 (1-4).

19. Y. Wang, K. Fujinami, R. Zhang, C. Wan, N. Wang, Y. Ba, K. Koumoto, Interfacial thermal resistance and thermal conductivity in nanograined $SrTiO_3$, *Appl. Phys. Express,* 2010. 3.

20. S. R. Yeandel, M. Molinari, S. C. Parker, Nanostructuring perovskite oxides: the impact of $SrTiO_3$ nanocube 3D self-assembly on thermal conductivity, *RSC Adv.,* 2016. 6: p. 114069-114077.

21. C. Yu, M. L. Scullin, M. Huijben, R. Ramesh, A. Majumdar, Thermal conductivity reduction in oxygen-deficient titanates, *Appl. Phys. Lett.,* 2008. 92.

22. A. Kikuchi, L. Zhang, N, Okinaka, T. Tosho, T. Akiyama, Optimization of sintering temperature for maximizing dimensionless figure of merit of La-doped strontium titanate thermoelectric material in the combination of combustion synthesis with post spark plasma sintering, *Materials Transactions,* 2010. 51 [10]: p. 1919-1922.

23. A. Kikuchi, N. Okinaka, T. Akiyama, A large thermoelectric thermoelectric figure of merit of La-doped $SrTiO_3$ prepared by combustion synthesis with post-spark plasma sintering, *Scripta Materialia,* 2010. 63: p. 407-410.

24. P. P. Shang, B. P. Zhang, Y. Liu, J. F. Li and H. M. Zhu, Preparation and thermoelectric properties of La-doped $SrTiO_3$ ceramics. *J. Electron. Mater.*, 2011. 40(5): p. 926 -931.

25. S. Ohta, H. Ohta, K. Koumoto, Grain size dependence of thermoelectric performance of Nb-doped $SrTiO_3$ polycrystals, *J. Ceram. Soc. of Japan,* 2006. 114 [1]: p. 102-105.

26. B. Zhang, J. Wang, T. Zou, S. Zhang, X. Yaer, N. Ding, C. Liu, L. Miao, Y. Li, Y. Wu, *J. Mater. Chem. C.,* 2015. p. 11406-11411.

27. N. Wang, H. Chen, H. He, W. Norimatsu, K. Koumoto, *Scientific Reports,* 2013. 3: p. 3449.

28. J.-B. Li, J. Wang, J.-F. Li, Y. Li, H. Yang, H.-Y. Yu, X.-B. Ma, X. Yaer, L. Liu, L. Miao, Broadening the temperature range for high thermoelectric performance of bulk polycrystalline strontium titanate by controlling the electronic transport properties, *J. Mater. Chem. C,* 2018. 6: p. 7594-7603.

29. F. Azough, S. S. Jackson, D. Ekren, R. Freer, M. Molinari, S. R. Yeandel, P. M. Panchmatia, S. C. Parker, D. H. Maldonado, D. M. Kepaptsoglou, and Q. M. Ramasse, Concurrent La and A-Site vacancy doping modulates the thermoelectric response of $SrTiO_3$: Experimental and computational evidence. *ACS Appl. Mater. Interfaces*, 2017. 9(48): p. 41988-42000.

30. D. Srivastava, C. Norman, F. Azough, M. C. Schäfer, E. Guilmeau, D. Kepaptsoglou, Q. M. Ramasse, G. Nicotra, R. Freer, Tuning the thermoelectric propertiesof A-site deficient $SrTiO_3$ ceramics by vacancies and carrier concentration, *Phys. Chem. Chem. Phys,* 2016. 18: p. 26475-26486.

31. C. J. Howard, G. R. Lumpkin, R. I. Smith, Z. Zhang, Crystal structures and phase transition in the system $SrTiO_3$-$La_{2/3}TiO_3$, *Journal of Solid State Chemistry,* 2004. 177: p. 2726-2732.

32. S. R. Popuri, A. J. M. Scott, R. A. Downie, M. A. Hall, E. Suard, R. Decourt, M. Pollet, J.-W. G. Bos, Glass-like thermal conductivity in $SrTiO_3$ thermoelectrics induced by A-site vacancies, *RSC Adv.*, 2014. 4: p. 33720-33723.

33. Z. Lu, H. Zhang, W. Lei, D. C. Sinclair, and I. M. Reaney, High-figure-of-merit thermoelectric La-doped A-site-deficient $SrTiO_3$ Ceramics. *Chem. Mater.*, 2016. 28: p. 925 - 935.

34. Y. Chen, J. Liu, X. Li, Y. Li, W. Su, J. Li, L. L. Zhao, C. L. Wang, M. Lu, Enhancement of thermoelectric performance of $Sr_{0.9-x}Nd_{0.1}Ti_{0.9}Nb_{0.1}O_3$ ceramics by introducing Sr vacancies, *Phys. Status Solidi A,* 2018. 215.

35. S. R. Popuri, R. Decourt, J. A. McNulty, M. Pollet, A. D. Fortes, F. D. Morrison, M. S. Senn, J. W. G. Bos, Phonon-glass and heterogeneous electrical transport in A-site deficient $SrTiO_3$, *J. Phys. Chem. C,* 2019. 123: p. 5198-5208.

36. J. C. Ruiz-Morales, J. Canales-Vazquez, C. Savaniu, D. Marrero-Lopez, W. Zhou, J. T. S. Irvine, Disruption of extended defects in solid oxide fuel cell anodes for methane oxidation, *Nature Lett.,* 2006. 439: p. 568-571.

37. T. E. Loland, J. Sele, M.-A. Einarsrud, P. E. Vullum, M. Johnsson, and K. Wiik, Thermal conductivity of A-site cation-deficient La-substituted $SrTiO_3$ produced by spark plasma sintering. *Energy Harvesting and Systems*, 2015. 2(1-2): p. 63-71.

38. I. Wærnhus, Defect chemistry, conductivity and mass transport properties of $La_{1-x}Sr_xFeO_3$ (x=0 and 0.1), PhD-thesis. Department of Materials Science and Engineering, Norwegian University of Science and Technology,NTNU, 2003, Trondheim, Norway.

39. D. A. H. Hanaor, and C. C. Sorell, Review of the anatase to rutile phase transformation. *J. Mater. Sci.*, 2011. 46(4): p. 855-874.18.

40. R. Moos, T. Bischoff, W. Menesklou, and K. H. Hardtl, Solubility of lanthanum in strontium titanate in oxygen-rich atmospheres. *J. Mater. Sci.*, 1997. 32(16): p. 4247-4252.

41. D. Neagu, J. T. S. Irvine, Structure and properties of $La_{0.4}Sr_{0.4}TiO_3$ ceramics for use as anode materials in solid oxide fuel cells, *Chem. Mater.,* 2010. 22: p. 5042-5053.

42. D. Burnat, A. Heel, L. Holzer, D. Kata, J. Lis, T. Graule, Synthesis and performance of A-site deficient lanthanum-doped strontium titanate by nanoparticle based spray pyrolysis, *Journal of Power Sources,* 2012. 201: p. 26-36.

43. R. Landauer, Electrical conductivity in inhomogeneous media. *AIP Conf. proc.,* 1978. 40(1): p. 2-45.

44. R. Moos, and K. H. Hardtl, Defect chemistry of donor-doped and undoped strontium titanate ceramics between 1000 and 1400°C. *J. Am. Ceram. Soc.*, 1997. 80(10): p. 2549-2562.

45. R. Moos, S. Schöllhammer, and K. H. Härdtl, Electron mobility of $Sr_{1-x}La_xTiO_3$ ceramics between 600 °C and 1300 °C. *Appl. Phys. A*, 1997. 65, p. 291-294.

46. P. Blennow, A. Hagen, K.Hansen, L. R. Wallenberg, and M. Mogensen, Defect and electrical transport properties of Nb-doped $SrTiO_3$. *Solid State Ionics*, 2008. 179(35): p. 2047-2058.

47. P. Roy, V. Pal, T. Maiti, Effect of spark plasma sintering (SPA) on the thermoelectric properties of $SrTiO_3$:15 at% Nb, *Ceramics International,* 2017. p. 12809-12813.

48. S. J. P. Longworth, K. M. Knowles, and R. E. D. Borkowski, The measurement and interpretation of electrostatic potential profiles across grain boundaries in strontium titanate. *J. Phys. Conf. Ser.*, 2006. 26: p. 235 - 238.

49. A. M. Dehkordi, S. Bhattacharya, T. Darroudi, J. W. Graff, U. Schwingenschlögl, H. N. Alshareef, T. M. Tritt, Large thermoelectric power factor in Pr-doped $SrTiO_{3-\delta}$ ceramics via grain-boundary-induced mobility enhancement, *Chem. Mater.,* 2014. p. 2478-2485.

50. G. J. Snyder and E. S. Toberer, Complex thermoelectric materials. *Nat. Mater*, 2008. 7(2): p. 105-114.